

Real-time inverse scattering for optical coherence tomography

Tyler S. Ralston^a, Daniel L. Marks^a, P. Scott Carney^a,
and Stephen A. Boppart^{a,b}

^aBeckman Institute for Advanced Science and Technology and
Department of Electrical and Computer Engineering,
University of Illinois at Urbana-Champaign,
405 North Mathews Ave., Urbana IL 61801;
^bDepartments of Bioengineering and Medicine,
University of Illinois at Urbana-Champaign, Urbana, IL 61801

ABSTRACT

We have developed and implemented a system which can acquire, process, and display the solution of the inverse scattering problem for optical coherence tomography (OCT) in real-time at frame rates of 2.25 fps for 512 X 1024 images. Frames which previously required 60 s to process, now take under 0.5 s, an improvement in processing speed by a factor of over 120 times. An efficient routine was designed which requires two interpolations of the columns, one one-dimensional real-to-complex fast Fourier transform (FFT) of the columns, and two two-dimensional FFTs. The limits to speed now rely on the parallelizability of the processing hardware. Our system provides quantitatively meaningful structural information from previously indistinguishable scattering intensities and provides proof of feasibility for future real-time systems.

Keywords: Optical coherence tomography, inverse scattering

1. INTRODUCTION

For a long time, advances in optical microscopy have relied on the design of physical optical elements to produce images of samples directly. However, recently, with the advent of scanning modalities such as optical coherence tomography^{1,2} (OCT), image quality is determined as much by algorithm development as the quality of optical elements. The use of computed imaging and synthetic aperture techniques³⁻⁷ has extended the capabilities of OCT and optical coherence microscopy⁸⁻¹⁰ (OCM). Such computed imaging techniques are derived from physics-based OCT scattering models. One of the recently demonstrated advantages is the ability to resolve features in the sample that are outside of the confocal region. Ultimately, a more quantitatively accurate and faithful representation of the sample structure is computed.

We demonstrate the real-time solution to the inverse scattering problem for optical coherence tomography (OCT), which allows us to reconstruct cellular features in tissues for light scattered outside of the focal plane orders of magnitude faster than previously reported⁵. These results demonstrate that all planes can be reconstructed with the same resolution as typically only found at the focus in OCT. Currently, OCT systems are implemented for real-time visualization which is useful for immediate feedback in time critical situations or for monitoring transient dynamics. The design of a real-time system to provide spatially-invariant resolution has the potential to be a tremendous benefit to the microscopy community.

2. MATHEMATICAL FORMULATION

We assume a linear relationship between the sample susceptibility η , and the measured signal S . Our method to solve the inverse problem is first to define the forward problem based on the physics of scattering,

$$S = K\eta, \quad (1)$$

*Further author information: (Send correspondence to S.A.B.)
S.A.B.: E-mail: boppart@uiuc.edu

where K is the operator for the OCT system connecting sample structure and signal. Next, unfiltered reconstruction obtained by application of operator adjoint is defined,

$$\eta_A = K^* S. \quad (2)$$

Following this, we diagonalize and apply the normal operator, $K^* K$. The combination of these leads to a relatively simple minimum norm solution,

$$\hat{\eta} = (K^* K)^{-1} K^* S. \quad (3)$$

Should we need to compensate for noise in the signal, then we can implement a Tikhonov regularized solution, i.e.

$$\hat{\eta} = (K^* K + \lambda L^* L)^{-1} K^* (K\eta + w), \quad (4)$$

where w is the additive noise in the collected signal and $K\eta + w$ is a representation of the OCT signal, S . Such a linear model is implicitly the result of taking the first Born approximation for the scattering. OCT is especially amenable to the first Born approximation since contributions from higher order scattering will tend to be delayed by a longer time and thus fall outside the coherence time of the reference.

The generic description above takes more specific form through analysis of our particular apparatus. The field is assumed to be described in the frequency domain by an ensemble of fields at frequencies

$$\omega = \frac{kc}{n}, \quad (5)$$

where n is the index of refraction. Each member of the ensemble is taken to be a Gaussian beam with beam waist given by

$$W_o(k) = \frac{\alpha}{k}. \quad (6)$$

where α is π divided by the NA of the output lens of the system. The beam profile in the waist plane is given by the expression

$$\tilde{g}_0(\mathbf{r}, k) = e^{-\frac{r^2}{2W_o^2(k)}} \quad (7)$$

The incident field at any point in the sample may be written in terms of the plane wave decomposition

$$g(\mathbf{r}' - \mathbf{r}_o, k) = \frac{1}{(2\pi)^2} \int d^2 q e^{i\mathbf{q} \cdot (\mathbf{r}' - \mathbf{r}_o)} \tilde{g}(\mathbf{q}, z - z_o, k). \quad (8)$$

where

$$\tilde{g}(\mathbf{q}, z, k) = e^{ik_z(\mathbf{q})z} \tilde{g}_0(\mathbf{q}, k), \quad (9)$$

$$k_z(\mathbf{q}) = \sqrt{k^2 - q^2}, \quad (10)$$

and

$$\tilde{g}_0(\mathbf{q}, k) = e^{-q^2 \frac{W_o^2(k)}{2}} = e^{-q^2 \frac{\alpha^2}{2k^2}}. \quad (11)$$

The backscattered field in the Born approximation is given by

$$U(\mathbf{r}, \mathbf{r}_o, k) = A(k) \int_V d^3 r' G(\mathbf{r}', \mathbf{r}, k) g(\mathbf{r}' - \mathbf{r}_o, k) \eta(\mathbf{r}'), \quad (12)$$

where \mathbf{r}_o is the transverse position of the beam, $G(\mathbf{r}', \mathbf{r}, k)$ is the Green's function, $g(\mathbf{r}' - \mathbf{r}_o, k)$ is the translated incident field, and $A^2(k)$ is the power spectral density.

The fiber is assumed to be single mode. The coupling efficiency of a field $U(\mathbf{r}, \mathbf{r}_o, k)$, into the fiber through the optical system is equal to the projection of the field (in the usual $L^2(\mathbf{R}^2)$ sense) onto the output mode of the system. Thus, the signal $S(\mathbf{r}_o, k)$ coupled back into the fiber over the surface of the aperture output/input plane $Surf$ is given by

$$S(\mathbf{r}_o, k) = \int_{Surf} d^2 r U(\mathbf{r}, \mathbf{r}_o, k) g(\mathbf{r} - \mathbf{r}_o, k). \quad (13)$$

Substituting Eq. (12) for $U(\mathbf{r}, \mathbf{r}_o, k)$, we obtain

$$S(\mathbf{r}_o, k) = A(k) \int_{Surf} d^2 r \int_V d^3 r' G(\mathbf{r}', \mathbf{r}, k) g(\mathbf{r}' - \mathbf{r}_o, k) \eta(\mathbf{r}') g(\mathbf{r} - \mathbf{r}_o, k). \quad (14)$$

The photodetector measures the interferometric cross-correlation between the reference and sample signals, Eq. (14), as the relative time delay between the two is varied. The reference field is well characterized and so S may be determined from the measurements and we will assume that S is our observable. The forward problem may be cast such that K takes a diagonal form. The Green's function $G(\mathbf{r}', \mathbf{r}, k)$ can be Fourier decomposed to be space invariant such that

$$G(\mathbf{r}', \mathbf{r}, k) = \frac{1}{(2\pi)^2} \int d^2 q e^{i\mathbf{q} \cdot (\mathbf{r} - \mathbf{r}')} \tilde{G}(\mathbf{q}, z - z', k), \quad (15)$$

For our case, the boundary of the surface area will be at $z_0 = 0$, and thus the signal becomes

$$S(\mathbf{r}_0, k) = \frac{A(k)}{(2\pi)^6} \int_{\text{surf}} d^2 r \int_V d^3 r' \int d^2 q \int d^2 q' \int d^2 q'' e^{i\mathbf{q} \cdot (\mathbf{r} - \mathbf{r}')} e^{i\mathbf{q}' \cdot (\mathbf{r}' - \mathbf{r}_0)} e^{i\mathbf{q}'' \cdot (\mathbf{r} - \mathbf{r}_0)} \tilde{G}(\mathbf{q}, z - z', k) \tilde{g}(\mathbf{q}', z', k) \tilde{g}(\mathbf{q}'', z, k) \eta(\mathbf{r}') \quad (16)$$

Now, integration can be done with respect to \mathbf{r} .

Note:

$$\frac{1}{(2\pi)^2} \int e^{i\mathbf{q} \cdot \mathbf{r}} d^2 r = \delta(\mathbf{q}). \quad (17)$$

$$S(\mathbf{r}_0, k) = \frac{A(k)}{(2\pi)^4} \int d^2 q \int d^2 q' \int d^2 q'' \int_V d^3 r' \delta(\mathbf{q} + \mathbf{q}'') e^{i\mathbf{q} \cdot (-\mathbf{r}')} e^{i\mathbf{q}' \cdot (\mathbf{r}' - \mathbf{r}_0)} e^{i\mathbf{q}'' \cdot (-\mathbf{r}_0)} \tilde{G}(\mathbf{q}, z - z', k) \tilde{g}(\mathbf{q}', z', k) \tilde{g}(\mathbf{q}'', z, k) \eta(\mathbf{r}') \quad (18)$$

Now, we can integrate with respect to \mathbf{r}' for the transverse coordinates leaving z' integration unchanged.

$$S(\mathbf{r}_0, k) = \frac{A(k)}{(2\pi)^2} \int d^2 q \int d^2 q' \int d^2 q'' \int dz' \delta(\mathbf{q} + \mathbf{q}'') e^{i\mathbf{q} \cdot (-\mathbf{r}_0)} e^{i\mathbf{q}' \cdot (-\mathbf{r}_0)} \tilde{G}(\mathbf{q}, z - z', k) \tilde{g}(\mathbf{q}', z', k) \tilde{g}(\mathbf{q}'', z, k) \tilde{\eta}(\mathbf{q}' - \mathbf{q}; z') \quad (19)$$

Using the sifting property of the delta function, we integrate over \mathbf{q}'' ,

$$S(\mathbf{r}_0, k) = \frac{A(k)}{(2\pi)^2} \int d^2 q \int d^2 q' \int dz' e^{i(\mathbf{q} - \mathbf{q}') \cdot \mathbf{r}_0} \tilde{G}(\mathbf{q}, z - z', k) \tilde{g}(\mathbf{q}', z', k) \tilde{g}(-\mathbf{q}, z, k) \tilde{\eta}(\mathbf{q}' - \mathbf{q}; z') \quad (20)$$

where $\tilde{\eta}(\mathbf{q}; z)$ is the Fourier transform of $\eta(\mathbf{r}; z)$. Taking the Fourier transform with respect to the last spatial coordinate, \mathbf{r}_0 , where

$$\tilde{S}(\mathbf{Q}, k) = \int S(\mathbf{r}_0, k) e^{-i\mathbf{Q} \cdot \mathbf{r}_0} d^2 r_0, \quad (21)$$

yields,

$$\tilde{S}(\mathbf{Q}, k) = A(k) \int d^2 q \int d^2 q' \int dz' \delta(\mathbf{q} - \mathbf{q}' - \mathbf{Q}) \tilde{G}(\mathbf{q}, z - z', k) \tilde{g}(\mathbf{q}', z', k) \tilde{g}(-\mathbf{q}, z, k) \tilde{\eta}(\mathbf{q}' - \mathbf{q}; z') \quad (22)$$

Integrate over spatial frequency component, \mathbf{q}' , and apply sifting theorem to get

$$\tilde{S}(\mathbf{Q}, k) = A(k) \int d^2 q \int dz' \tilde{G}(\mathbf{q}, z - z', k) \tilde{g}(\mathbf{q} + \mathbf{Q}, z', k) \tilde{g}(-\mathbf{q}, z, k) \tilde{\eta}(\mathbf{Q}; z') \quad (23)$$

Now, find the Fourier decomposition of the full volume

$$\mathbf{g}(\mathbf{r}, k) = \frac{1}{(2\pi)^2} \int d^2 q e^{i\mathbf{q} \cdot \mathbf{r}} \tilde{g}(\mathbf{q}, z, k), \quad (24)$$

and

$$\mathbf{g}(\mathbf{r}, k) = \frac{1}{(2\pi)^2} \int d^2 q e^{i\mathbf{q} \cdot \mathbf{r}} e^{ik_z(\mathbf{q})z} \int_{z=0} d^2 r' \mathbf{g}(\mathbf{r}', k) e^{-i\mathbf{q} \cdot \mathbf{r}'} \quad (25)$$

Thus,

$$\tilde{g}(\mathbf{q}, z, k) = e^{ik_z(\mathbf{q})z} \int_{z=0} d^2 r' \mathbf{g}(\mathbf{r}', k) e^{-i\mathbf{q} \cdot \mathbf{r}'}. \quad (26)$$

Without loss of generality, we can assume the measurement plane is at $z = 0$. Thus,

$$\tilde{S}(\mathbf{Q}, k) = A(k) \int d^2 q \int dz' e^{ik_z(\mathbf{q} + \mathbf{Q})z'} \tilde{G}(\mathbf{q}, -z', k) \tilde{g}(\mathbf{q} + \mathbf{Q}, k) \tilde{g}(-\mathbf{q}, k) \tilde{\eta}(\mathbf{Q}; z'). \quad (27)$$

Although not done here, notice that any position z_0 can be incorporated into Eq. (27) as shown in reference 3.

For each transverse wave vector you get a phase component, shown by

$$\tilde{G}(\mathbf{r}-\mathbf{r}',k) = \frac{1}{(2\pi)^2} \int d^2q \tilde{G}(\mathbf{q},z-z',k) e^{i\mathbf{q}(\mathbf{r}-\mathbf{r}')}, \quad (28)$$

and

$$\tilde{G}(\mathbf{r}-\mathbf{r}',k) = \frac{i}{2\pi} \int d^2q \frac{1}{k_z(\mathbf{q})} e^{i\mathbf{q}(\mathbf{r}-\mathbf{r}')} e^{-ik_z(\mathbf{q})(z-z')}. \quad (29)$$

Thus, the angular spectrum amplitude of the free space Green's function is given by the expression,

$$\tilde{G}(\mathbf{q},z-z',k) = \frac{i2\pi}{k_z(\mathbf{q})} e^{-ik_z(\mathbf{q})(z-z')}. \quad (30)$$

The signal coupled back into the fiber now becomes:

$$\tilde{S}(\mathbf{Q},k) = A(k) \int d^2q \int dz' \frac{i2\pi}{k_z(\mathbf{q})} e^{ik_z(\mathbf{q})z'} e^{ik_z(\mathbf{q}+\mathbf{Q})z'} \tilde{g}(\mathbf{q}+\mathbf{Q}) \tilde{g}(-\mathbf{q}) \tilde{\eta}(\mathbf{Q};z') \quad (31)$$

Remember that for the longitudinal wave vector

$$k_z(\mathbf{q}) = \sqrt{k^2 - q^2}. \quad (32)$$

Notice that $k_z(\mathbf{q})$ is an even symmetric function so that

$$k_z(\mathbf{q}) = k_z(-\mathbf{q}). \quad (33)$$

By separating terms and transforming $\mathbf{q} \leftrightarrow -\mathbf{q}$, a convolution sum can be formed,

$$\tilde{S}(\mathbf{Q},k) = A(k) \int d^2q \int dz' \frac{i2\pi}{k_z(\mathbf{q})} \left[e^{ik_z(\mathbf{q})z'} \tilde{g}(\mathbf{q},k) \right] \left[e^{ik_z(\mathbf{Q}-\mathbf{q})z'} \tilde{g}(\mathbf{Q}-\mathbf{q},k) \right] \tilde{\eta}(\mathbf{Q};z'). \quad (34)$$

The convolution of two functions of the form,

$$\tilde{f}(\mathbf{q},k) = e^{ik_z(\mathbf{q})z} \tilde{g}(\mathbf{q},k), \quad (35)$$

and

$$\tilde{h}(\mathbf{q},k) = k_z(\mathbf{q},k)^{-1} \tilde{f}(\mathbf{q},k), \quad (36)$$

can be described by

$$H(\mathbf{q},k) = (\tilde{f} * \tilde{h})(\mathbf{q},k), \quad (37)$$

which finally gives us

$$\tilde{S}(\mathbf{Q},k) = i2\pi A(k) \int dz' H(\mathbf{Q},z',k) \tilde{\eta}(\mathbf{Q};z'). \quad (38)$$

where

$$H(\mathbf{Q},z,k) = \int d^2q \frac{1}{k_z(\mathbf{q})} \left[e^{ik_z(\mathbf{q})z} \tilde{g}(\mathbf{q},k) \right] \left[e^{ik_z(\mathbf{Q}-\mathbf{q})z} \tilde{g}(\mathbf{Q}-\mathbf{q},k) \right]. \quad (39)$$

From this point, there are several methods to approximate a solution which diagonalizes the operators K and K^* . In OCT, making the paraxial approximation³ provides adequate results, thus the calculations will be carried out with the paraxial approximation first and then related to the solutions using the non-paraxial equivalent solution⁴. In the paraxial approximation, the factor $k_z(\mathbf{q}) \approx k$ in Eq. (36) so that the following simplification is made:

$$H(\mathbf{q},k) = k^{-1} (\tilde{f} * \tilde{f})(\mathbf{q},k) \quad (40)$$

where

$$\tilde{f}(\mathbf{q},k) = e^{ik_z(\mathbf{q})z} \tilde{g}(\mathbf{q},k). \quad (41)$$

Using Parseval's theorem, Eq. (38) reduces to a relatively simple spatial relationship.

$$S(\mathbf{r}_0,k) = i2\pi k^{-1} A(k) \int d^3r f(\mathbf{r}-\mathbf{r}_0,k)^2 \eta(\mathbf{r}) \quad (42)$$

where,

$$f(\mathbf{r},k) = (2\pi)^{-2} \int d^2q e^{i\mathbf{q}\cdot\mathbf{r}} \tilde{f}(\mathbf{q},k). \quad (43)$$

Incorporating the Gaussian beam's frequency-dependent waist size, Eq. (11), yields the following:

$$\tilde{f}(\mathbf{q},k) = e^{iz\sqrt{k^2-q^2}} e^{-q^2 \frac{\alpha^2}{2k^2}} \quad (44)$$

where $k = \frac{\omega n}{c}$. Note that in the Fresnel Zone the follow approximation can be used:

$$\sqrt{k^2 - q^2} \approx k - \frac{1}{2} \frac{q^2}{k} \quad (45)$$

Thus,

$$\tilde{f}(\mathbf{q}, k) = e^{izk} e^{-q^2 \left(\frac{\alpha^2}{2k^2} + i \frac{z}{k} \right)}. \quad (46)$$

Now take the Fourier transform to simplify the convolution. The Fourier transform pair for a Gaussian is

$$e^{-\frac{q^2 b^2}{2}} \xleftrightarrow{\mathcal{F.T.}} |b|^{-2} e^{-\frac{r^2}{2b^2}}, \quad (47)$$

which implies that

$$\tilde{f}(\mathbf{q}, k) = e^{izk} e^{-\frac{q^2}{2} \left(\frac{\alpha^2}{k^2} + i \frac{z}{k} \right)} \xleftrightarrow{\mathcal{F.T.}} f(\mathbf{r}) = \left(\frac{\alpha^2}{k^2} + i \frac{z}{k} \right)^{-1} e^{izk} e^{-\frac{r^2}{2} \left(\frac{\alpha^2}{k^2} + i \frac{z}{k} \right)^{-1}}. \quad (48)$$

and square since convolution in the spatial frequency domain is equivalent to multiplication in the spatial domain,

$$f(\mathbf{r}, k)^2 = e^{2izk} e^{-\frac{r^2}{2} \left(\frac{\alpha^2}{2k^2} + i \frac{z}{2k} \right)^{-1}}. \quad (49)$$

Now, by taking the inverse Fourier transform, the kernel H takes the form

$$H(\mathbf{q}, k) = k^{-1} (\tilde{f} * \tilde{f})(\mathbf{q}, k) = \frac{1}{4\pi} \left(\frac{\alpha^2}{k} + iz \right)^{-1} e^{2izk} e^{-\frac{q^2}{2} \left(\frac{\alpha^2}{2k^2} + i \frac{z}{2k} \right)^{-1}}. \quad (50)$$

It is convenient to introduce the following notation

$$I(k) \equiv \frac{1}{4\pi} \left(\frac{\alpha^2}{k} + iz \right)^{-1}. \quad (51)$$

Represented in terms of transverse spatial frequency coordinates, we can formulate the forward problem over an orthogonal transverse spatial frequency space. We reformulate Eq. (38) as a type one Fredholm integral equation, so that the kernel of the operator K is apparent,

$$\tilde{S}(\mathbf{Q}, k) = K \tilde{\eta}(\mathbf{Q}'; z') = i2\pi A(k) \int dz' \int d^2 Q' \delta^{(2)}(\mathbf{Q} + \mathbf{Q}') H(-\mathbf{Q}', z', k) \tilde{\eta}(\mathbf{Q}'; z'). \quad (52)$$

In this representation the kernel is diagonal. Next, we incorporate the spatial frequency dependence, k , and the expression for $H(-\mathbf{Q}', z', k)$, a part of which is the Gaussian beam constraint,

$$\tilde{S}(\mathbf{Q}, k) = K \tilde{\eta}(\mathbf{Q}'; z') = i2\pi A(k) \int dz' \int d^2 Q' \delta^{(2)}(\mathbf{Q} + \mathbf{Q}') I(k) e^{2iz'k} e^{-\frac{Q'^2}{4} \left(\frac{\alpha^2}{k^2} + i \frac{z'}{k} \right)} \tilde{\eta}(\mathbf{Q}'; z'). \quad (53)$$

By taking the Fourier transform with respect to z' , substituting $\tilde{\eta}(\mathbf{Q}'; z') = \frac{1}{2\pi} \int d\beta e^{i\beta z'} \tilde{\eta}(\mathbf{Q}', \beta)$, we obtain,

$$\tilde{S}(\mathbf{Q}, k) = iA(k) \int d\beta \int d^2 Q' \delta^{(2)}(\mathbf{Q} + \mathbf{Q}') I(k) \delta\left(\beta - \left(\frac{Q'^2}{4k} - 2k\right)\right) e^{-\frac{Q'^2 \alpha^2}{4k^2}} \tilde{\eta}(\mathbf{Q}', \beta), \quad (54)$$

where

$$I(k) = \frac{1}{4\pi} \left(\frac{\alpha^2}{k} + iz \right)^{-1}. \quad (55)$$

The adjoint solution then is defined by applying the adjoint of the linear operation found in (54),

$$\tilde{\eta}_A(\mathbf{Q}'', \beta) = -i2\pi \int dk d^2 Q \delta(\mathbf{Q} + \mathbf{Q}'') I(k) A(k) \delta\left(2k + \beta - \frac{Q''^2}{4k}\right) e^{-\frac{Q''^2 \alpha^2}{4k^2}} \tilde{S}(\mathbf{Q}, k). \quad (56)$$

Which may be seen to be equivalent to

$$\tilde{\eta}_A(\mathbf{Q}, \beta) = -i2\pi \left(2 + \frac{Q^2}{4k^2}\right)^{-1} A(k) e^{\frac{Q^2 \alpha^2}{4k^2}} \tilde{S}(\mathbf{Q}, k) I(k) \Big|_{k=\frac{1}{2}\left(\frac{\beta}{2} + \sqrt{\left(\frac{\beta}{2}\right)^2 + \frac{Q^2}{2}}\right)}. \quad (57)$$

The normal operator can be written

$$K^* K(\mathbf{Q}', \beta, \mathbf{Q}, k) = (2\pi A(k))^2 \delta(\mathbf{Q} - \mathbf{Q}') \delta(k - \beta) I(k)^2 \left(2 + \frac{Q'^2}{4k^2}\right)^{-2} e^{-\frac{2Q'^2 \alpha^2}{4k^2}} \Big|_{k=\frac{1}{2}\left(\frac{\beta}{2} + \sqrt{\left(\frac{\beta}{2}\right)^2 + \frac{Q^2}{2}}\right)}. \quad (58)$$

Thus, the pseudo inverse is written

$$\tilde{\eta}^+(\mathbf{Q}, \beta) = (-i2\pi A(k) I(\mathbf{Q}, k))^{-1} \left(2 + \frac{Q^2}{4k^2}\right)^{-1} e^{i\pi_0 \left(2k - \frac{Q^2}{4k}\right)} \tilde{S}(\mathbf{Q}, k) \Big|_{k=\frac{1}{2}\left(\frac{\beta}{2} + \sqrt{\left(\frac{\beta}{2}\right)^2 + \frac{Q^2}{2}}\right)}. \quad (59)$$

The corresponding non-paraxial solution⁴ for the forward model is given by

$$\tilde{S}(\mathbf{Q}, k) = \frac{k^2}{\alpha^2} i2\pi^2 A(k) \frac{e^{-2ik_z(\mathbf{Q}/2)z_0}}{k_z(\mathbf{Q}/2)} e^{-\frac{\alpha^2 Q^2}{4k^2}} \tilde{\eta}[\mathbf{Q}, -2k_z(\mathbf{Q}/2)], \quad (60)$$

where $\tilde{\eta}$ is the three-dimensional Fourier transform of η . It may be noted that solution is distinct from the paraxial approximated solution (essentially a small $|\mathbf{q}|$ expansion of $k_z(\mathbf{q})$) which fails as $NA \rightarrow 1$. The kernel of the forward operator of the non-paraxial solution is given by

$$H(\mathbf{Q}, k, \beta) = \frac{k^2}{\alpha^2} i2\pi^2 A(k) \frac{e^{-2ik_z(\mathbf{Q}/2)z_0}}{k_z(\mathbf{Q}/2)} e^{-\frac{\alpha^2 Q^2}{4k^2}} \delta[\beta + 2k_z(\mathbf{Q}/2)], \quad (61)$$

where $\tilde{S}(\mathbf{Q}, k) = \int d\beta H(\mathbf{Q}, k, \beta) \tilde{\eta}(\mathbf{Q}, \beta)$. The kernel of the normal operator is given by the expression

$$H^* H(\mathbf{Q}, \beta, \beta') \equiv |f(\mathbf{Q}, 1/2\sqrt{\beta^2 + Q^2}, \beta)|^2 \frac{\beta}{2\sqrt{\beta^2 + Q^2}} \delta(\beta - \beta'), \quad (62)$$

where

$$f(\mathbf{Q}, k, \beta) = \frac{k^2}{\alpha^2} i2\pi^2 A(k) \frac{e^{-2ik_z(\mathbf{Q}/2)z_0}}{k_z(\mathbf{Q}/2)} e^{-\frac{\alpha^2 Q^2}{4k^2}}. \quad (63)$$

The kernel of the Tikhonov regularized pseudo-inverse with a regularization constant N is given by the expression

$$H^+(\mathbf{Q}, k; \beta) = \frac{f^*(\mathbf{Q}, k, \beta) \delta\left(k - 1/2\sqrt{\beta^2 + Q^2}\right)}{|f(\mathbf{Q}, k, \beta)|^2 + 2Nk/k_z(\mathbf{Q}/2)}. \quad (64)$$

The object structure is then given by the pseudo inverse solution

$$\tilde{\eta}^+(\mathbf{Q}, \beta) = \left[\frac{f^*(\mathbf{Q}, k, \beta) \tilde{S}(\mathbf{Q}, k)}{|f(\mathbf{Q}, k, \beta)|^2 + 2Nk/k_z(\mathbf{Q}/2)} \right]_{k=\frac{1}{2}\sqrt{\beta^2 + Q^2}} \quad (65)$$

The object structure in the coordinate domain is obtained by applying the three-dimensional inverse Fourier transform. Figure 1 displays the relationship between the resampling variables, Fig. 1 (a), and the resampling grid, Fig. 1 (b).

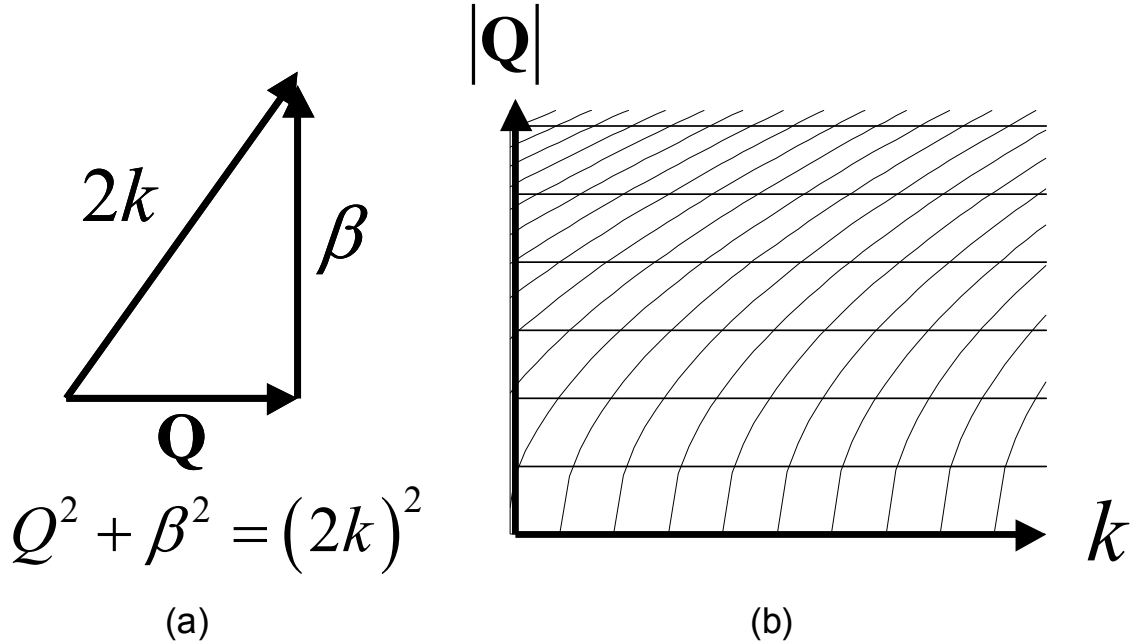


Fig. 1. (a) A relation between the spatial frequencies of the signal space and the spatial frequencies in the object space. (b) Sampling lattice for selected $(\beta, |\mathbf{Q}|)$ values on a uniform $(k, |\mathbf{Q}|)$ grid.

3. EXPERIMENTAL METHODOLOGY

Coherence imaging measurements are made using a spectral-domain OCT system, Figure 2. A femtosecond laser (Kapteyn-Murnane Laboratories, Boulder, CO), Figure 2a provides the broadband illumination. The bandwidth of the source is 100 nm, with a center wavelength of 800 nm. The first-order field quantities fluctuate too rapidly to be detected directly, thus the optical signal must be launched into an optical fiber-based Michelson interferometer, Figure 2b. The illuminating source is divided by a 50:50 fiber-optic coupler (splitter) for interference measurements and a 90:10 coupler for reference spectrum measurements. The reference arm contains a delay mirror and the sample arm contains a lens (objective) to focus the Gaussian beam into the sample, Figure 2c and 2d, respectively. In the sample arm, the objective has a focal length of 12 mm, a spot size of 5.6 μm , a confocal parameter (depth-of-focus) of 239 μm , and a NA of 0.05. The spectral detector collects light from the sample and reference arms, Figure 2e. In the spectrometer, the light is collimated with a 100 mm focal length achromatic lens and dispersed from a blazed gold diffraction grating (53004BK02-460R, Spectra-Physics), with 830.3 grooves per millimeter and a blaze angle of 19.70 degrees for a blaze wavelength of 828 nm. The dispersed optical spectrum is focused using a pair of achromatic lenses each having a focal length of 300 mm. The focused light is incident upon a line-scan camera (P2-2x-02K40, Dalsa.) which contains a 2048-element charge-coupled device (CCD) linear array with 10 x 10 μm detection elements. The camera operates at a readout rate of over 29 kHz, thus one axial scan can be captured during an exposure interval of about 34 μs . The tissue phantom was placed on a stage and the 2-D image data was acquired by scanning the incident beam in the transverse plane using a pair of computer-controlled galvanometer-scanning mirrors. The frame rate depends on the number of axial scans acquired per image or volume. In our experiment, a series of spectra images (500 X 2048 pixels) was each acquired in 17 ms. In Figure 2f, a frame capture card (PCI-1428, National Instruments, Inc.), collects camera data and writes it to the RAM. The frame capture card receives an external trigger from a galvanometer controller card (PCI-6711, National Instruments, Inc.) which activates the frame acquisition. The system CPUs are dual Intel Xeon processors operating at 3.0 GHz each.

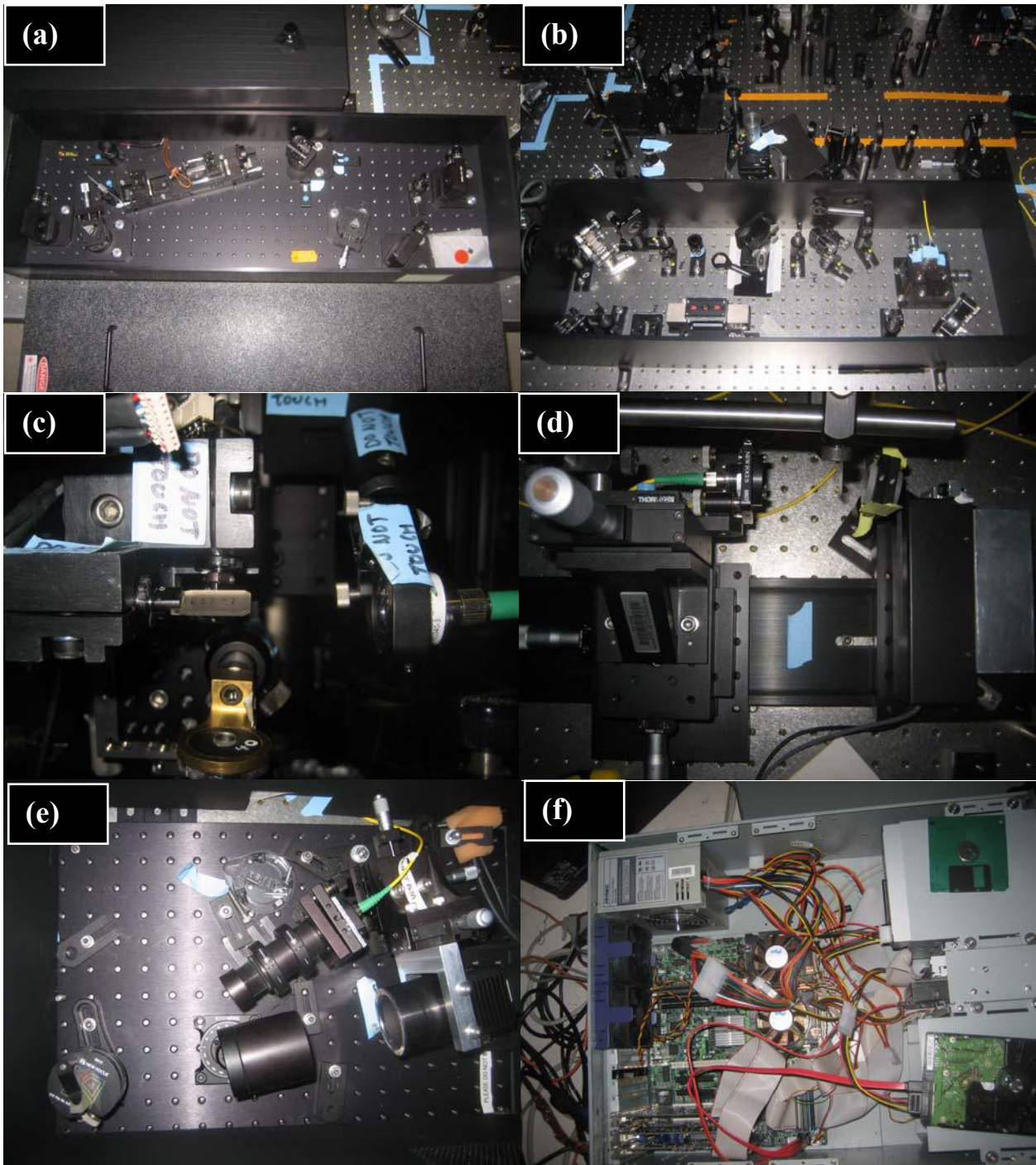


Fig. 2. (a) Ti:Sa laser. (b) Isolator and fiber optic launch. (c) Sample arm. (d) Reference arm. (e) Spectral detector. (f) Dual processor server.

A real-time system has been developed and implemented which can acquire, process, and display the inverse scattering solution for OCT in real-time at frame rates of 2.25 fps for 512 x 1024 images. Frames which previously required 60 s, now take under 500 ms, an improvement in processing speed by a factor of over 120 times. The improvements are due to a number of factors initially added for cautious prototyping including, but not limited to, the following:

1. Time-expensive commands in Matlab were used for interpolation.
2. Interpolation routines were in Matlab scripts with 'for' loops rather than vectorized or compiled.
3. Images were oversampled between 2 and 3 times as much as necessary.
4. All calculations were using double precision instead of float.
5. All scans were phase stabilized whether they required this or not.
6. Coefficients of resampling were computed during each execution, when they could be precomputed.

The new design is an efficient routine which requires two interpolations of the columns, one one-dimensional (1D) real-to-complex (R2C) fast Fourier transform (FFT) of the columns, and two 2D FFTs. Figure 3 shows the data flow chart starting with data acquired from the spectral-domain OCT system. The processing is designed similar to the tables in reference 3 except that the non-paraxial solution from reference 4 is used. Interpolation with cubic B -splines was used for both dispersion compensation and the inverse scattering solution. The FFT routine from the Intel Math Kernel Library (MKL) was used for all 1D and 2D transforms. The 1D FFT used 2048×512 real values, while the 2D FFTs used 1024×512 complex values. $S(r,t)$ is shifted by half such that the focus will be placed at the edge of the image. $S(r,t)$ is zeroed for values near DC to remove the noise caused by the average intensity on the detector. Memory was preallocated, and interpolation coefficients were precomputed.

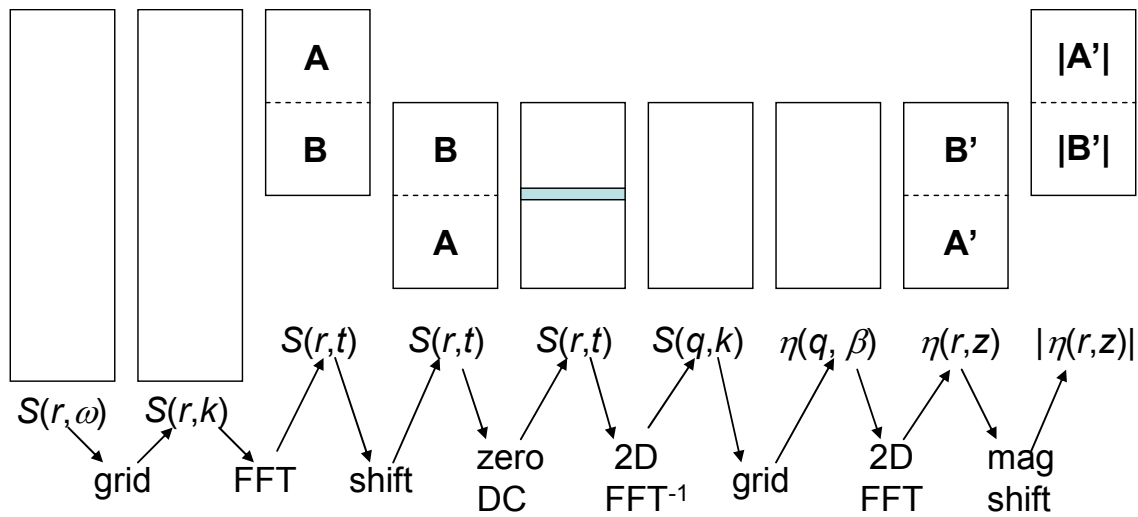


Fig. 3. Computational flow chart for memory allocation for each step of the inverse scattering algorithm.

We have imaged a tissue phantom and are able to determine previously indistinguishable scatterers from the reconstruction. The reconstruction better represents the tissue phantom and thus, provides better visualization and a potential for more accurate tissue classification and disease diagnosis. Our system provides quantitatively meaningful structural information from previously indistinguishable scattering intensities and provides proof of feasibility for future real-time systems. Figure 4 shows a screen shot of the data captured from the real-time OCT and 2D inverse scattering system. The future limits to speed are now reliant on the parallelizability of the processing hardware. The system provides quantitatively meaningful structural information from previously indistinguishable scattering intensities and provides proof of feasibility for future real-time systems.

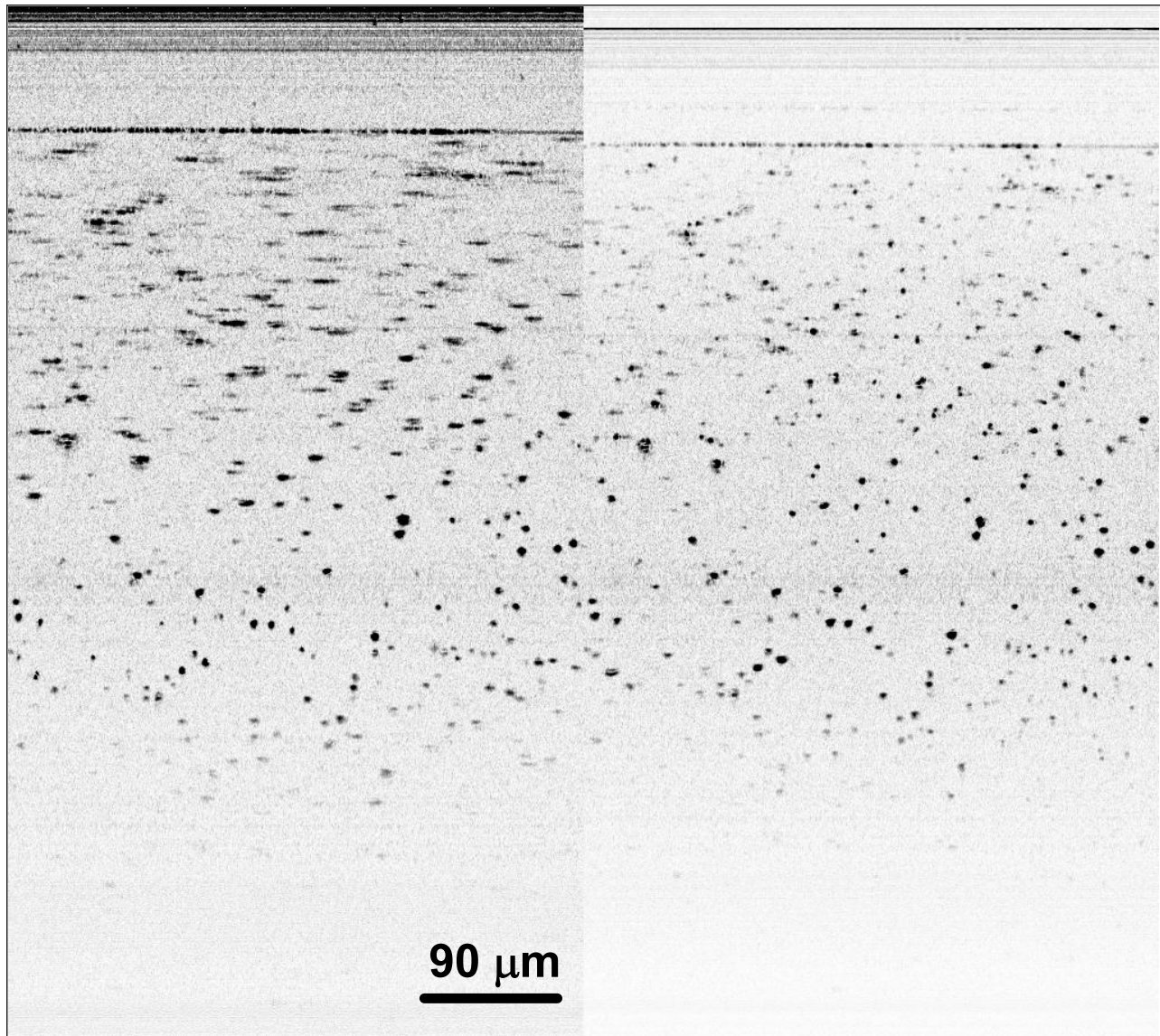


Fig. 4. Tissue phantom imaged with real-time inverse scattering OCT system. The original OCT image (left) and the inverse scattering solution (right) are computed in real-time.

4. CONCLUSIONS

Through modifications of reconstruction algorithm and hardware upgrades, we have demonstrated the feasibility for real-time imaging of the inverse scattering solution. The system described achieves spatially invariant resolution for all depths in a cross-sectional scan. Such a system has a potential to provide important cellular scattering information when used to image biological tissues. Furthermore, existent OCT systems may be modified to produce similar results with only minor modifications to the processing algorithm.

REFERENCES

1. D. Huang, E. A. Swanson, C. P. Lin, J. S. Schuman, W. G. Stinson, W. Chang, M. R. Hee, T. Flotte, K. Gregory, C. A. Puliafito, and J. G. Fujimoto, "Optical Coherence Tomography," *Science* **254**(5035), pp. 1178–1181, 1991.

2. S. A. Boppart, B. E. Bouma, C. Pitris, J. F. Southern, M. E. Brezinski, and J. G. Fujimoto, "In vivo cellular optical coherence tomography imaging," *Nature Medicine* **4**, pp. 861–864, 1998.
3. T. S. Ralston, D. L. Marks, P. S. Carney, and S. A. Boppart, "Inverse scattering problem for optical coherence tomography," *J. Opt. Soc. Am. A* **23**, pp. 1027–1037, 2006.
4. T. S. Ralston, D. L. Marks, S. A. Boppart, and P. S. Carney, "Inverse scattering for high-resolution interferometric microscopy," *Opt. Lett.* **24**, pp. 3585–3587, 2006.
5. T. S. Ralston, D. L. Marks, P. S. Carney, and S. A. Boppart, "Interferometric synthetic aperture microscopy," *NaturePhys.* **in press**, 2007.
6. D. L. Marks, T. S. Ralston, P. S. Carney, and S. A. Boppart, "Inverse scattering for rotationally scanned optical coherence tomography," *J. Opt. Soc. Am. A* **23**, pp. 2433–2439, 2006.
7. D. L. Marks, T. S. Ralston, P. S. Carney, and S. A. Boppart, "Inverse scattering for frequency-scanned full-field optical coherence tomography," *J. Opt. Soc. Am. A* **in press**, 2007.
8. J. A. Izatt, M. R. Hee, G. M. Owen, E. A. Swanson, and J. G. Fujimoto, "Optical coherence microscopy in scattering media," *Opt. Lett.* **19**, pp. 590–592, 1994.
9. J. M. Schmitt, M. J. Yadlowsky, and R. F. Bonner, "Subsurface imaging of living skin with optical coherence microscopy," *Dermatology* **191**, pp. 93–98, 1995.
10. J. A. Izatt, H.-W. Kulkarni, K. Wang, M. W. Kobayashi, and M. W. Sivak, "Optical coherence tomography and microscopy in gastrointestinal tissues," *IEEE J. Selected Topics in Quantum Elect.* **2**, pp. 1017–1028, 1996.